Simultaneous identification of elastic properties, thickness, and diameter of arteries excited with ultrasound radiation force

Parikshit Dutta[1], Matthew W. Urban[2], Olivier P. Le Maître[3], James F. Greenleaf[2] and Wilkins Aquino[1],

1. Department of Civil and Environmental Engineering, Duke University,
121 Hudson Hall, Durham, NC, 27708
2. Physiology and Biomedical Engineering, Mayo Clinic College of Medicine,
200 First Street Southwest, Rochester, MN, 55905
3. LIMSI-CNRS, Orsay, France

Abstract. The elastic and geometric properties of arteries have been long recognized as important predictors of cardiovascular disease. This work presents a robust technique for the noninvasive characterization of anisotropic elastic properties as well as thickness and diameter in arterial vessels. In our approach, guided waves are excited along arteries using the radiation force of ultrasound. Group velocity is used as the quantity of interest to reconstruct elastic and geometric features of the vessels. One of the main contributions of this work is a systematic approach based on sparse-grid collocation interpolation to construct surrogate models of arteries. These surrogate models are in turn used with direct-search optimization techniques to produce fast and accurate estimates of elastic properties, diameter, and thickness. One of the attractive features of the proposed approach is that once a surrogate model is built, it can be used for near real-time identification across many different types of arteries. We demonstrate the feasibility of the method using simulated and *in vitro* laboratory experiments on a silicon rubber tube and a porcine carotid artery. Our results show that using our proposed method, we can reliably identify the longitudinal modulus, thickness, and diameter of arteries. The circumferential modulus was found to have little influence in the group velocity, which renders the former quantity unidentifiable using the current experimental setting. Future work will consider the measurement of circumferential waves with the objective of improving the identifiability of the circumferential modulus.

1. Introduction

The elastic properties of arteries have received significant attention in recent years as they have been identified as independent predictors of cardiovascular health (Blacher et al. 1998). Moreover, in recent years, geometric quantities such as the intima-media thickness have been also identified as early indicators of cardiovascular disease (Davis et al. 1999, Polak et al. 2011). In this regard, noninvasive methods for estimating material and geometric properties in arteries are of great current interest.

Several methods have been proposed recently for the non-invasive characterization of elastic modulus in arteries such as measurement of the speed of propagation of pressure waves (Cockcroft et al. 2005), direct analysis of propagating modes (Bernal et al. 2011, Zhang et al. 2005, Luo et al. 2012, Konofagou et al. 2011, Luo et al. 2009, Couade et al. 2010), and inverse problem strategies based on the finite element method (Rosario et al. 2008), among others. On the other hand, the thickness of arteries is usually estimated through angiography, which is an invasive procedure, or from direct measurements in ultrasound images. The latter approach is subject to operator error and may yield significant variability of results. To the best knowledge of the authors, methodologies for the simultaneous estimation of elastic properties and thickness in arteries have yet to be developed.

The main goal of this work is to devise a fast and accurate methodology for the noninvasive characterization of anisotropic elastic properties, thickness, and diameter of arteries. To this end, in our approach, arteries are excited with ultrasound radiation (US) force and the normal particle velocity is measured along the length of the artery. The material properties and geometry (i.e. thickness and diameter) of the artery are estimated using an inverse problem solved in a constrained optimization framework. One of the main theoretical contributions of this work is the construction of surrogate models of the acoustic-structure interaction system using a sparse grid collocation approach to accelerate the inversion process. The notion is that once a surrogate is created, it can be used for the expedient reconstruction of material and geometric properties across many different arteries.

Numerical optimization approaches are becoming more frequently used for estimating material properties in biomedical applications (Aguilo et al. 2010, Oberai et al. 2003, Arridge & Hebden 1997). The main drawback of these approaches is the computational expense and complexity of implementation. For instance, finite elements are commonly used to discretize the forward problem, which has to be solved repeatedly during the optimization process. For medical diagnosis problems, such as the ones pursued in this work, minimization of computational time is highly desirable.

Different alternatives exist to decrease computational time, while maintaining accuracy in the solution of the inverse problem. For instance, model reduction approaches have been proposed and successfully used for inverse materials identification (Deng & Edwards 2007). Some approaches reduce the dimension of the approximation spaces such as those based on the Proper Orthogonal Decomposition (POD) (Brigham

et al. 2007). Although POD has been successfully used to solve many important problems, one key aspect for success with POD is coming up with adequate data (i.e. snapshots) for obtaining a suitable basis for a given problem. To this end, a general and effective strategy is still needed.

Other model reduction approaches adopt a non-intrusive approach in which maps between parameter spaces (e.g. material and geometric features) and state variable spaces (e.g. displacements, velocities, etc.) are constructed (Brigham & Aquino 2007, Aguilo et al. 2010). These maps have been developed using different techniques such as neural networks, support vector machines, radial basis functions, wavelets, and polynomials, among many others (Bishop 2006). The main advantage of using this type of surrogate model is the non-intrusive nature as they can be constructed off-line. In this work, surrogate models are constructed using polynomial interpolation along with a Smolyak's sparse grid collocation strategy (Smolyak 1963, Nobile et al. 2008, Ganapathysubramanian & Zabaras 2007, Xiu & Hesthaven 2005, Klimke et al. 2004). The main advantages of polynomial interpolation on sparse grids are readily available error estimates and ease of training. In this work, arteries will be represented as cylindrical geometries with transversely isotropic materials, allowing for low-dimensional parametric representations of both geometry and material properties.

This paper is organized as follows: Section 2 describes the forward problem, a method for calculating group velocity, the sparse grid collocation technique, and the algorithm proposed for inverse identification. In Section 3, we present numerical examples that demonstrate the performance of the method using simulated experiments. In Section 4, we present experimental results for an *in vitro* artery and a rubber tube. Finally Section 5 states the conclusions and future work.

2. Background

2.1. Forward Model

In this work, we model an artery and the surrounding fluid as a coupled acoustic-structure interaction (ASI) dynamical system. The governing equations for an artery undergoing time-harmonic motion are given as

$$\rho_s \ddot{\mathbf{u}} - \nabla \cdot \boldsymbol{\sigma} = \mathbf{0}, \qquad \text{in } \Omega_s \qquad (1a)$$

$$\mathbf{u}|_{t=0} = \mathbf{0}, \quad \dot{\mathbf{u}}|_{t=0} = \mathbf{0} \qquad \text{in } \Omega_s \qquad (1b)$$

$$\boldsymbol{\epsilon}[\mathbf{u}] = \frac{1}{2}(\nabla \mathbf{u} + \nabla \mathbf{u}^\top), \qquad \text{in } \Omega_s, \qquad (1c)$$

$$\boldsymbol{\sigma} = \mathbb{C} : \epsilon, \qquad \text{in } \Omega_s \qquad (1d)$$

$$\boldsymbol{\sigma} \mathbf{n}_s = -p \mathbf{n}_s, \qquad \text{on } \Gamma_{fs} \qquad (1e)$$

$$\boldsymbol{\sigma} \mathbf{n}_s = \boldsymbol{\tau}, \qquad \text{on } \Gamma_t \qquad (1f)$$

$$\boldsymbol{B} \mathbf{u} = \mathbf{0}, \qquad \text{on } \Gamma_R \qquad (1g)$$

where $\mathbf{u}$ is displacement, $\boldsymbol{\sigma}$ is the stress tensor, ρ_s is the solid mass density. The variable Ω_s represents the solid medium, which in the present case is the artery, $\boldsymbol{\epsilon}$ is the linearized strain tensor and $\mathbb{C}$ is the elasticity tensor. The boundary at the interface of the artery and fluid is represented as Γ_{fs}, while Γ_t is the part of the boundary where tractions are applied, and $\mathbf{n}_s$ is a unit vector normal to the surface of the solid. The operator $\boldsymbol{B}$ is used to represent absorbing conditions on the boundary Γ_R. In this work, we used a Perfectly Matched Layer (PML) formulation to approximate non-absorbing conditions in the solid domain. Details of PML formulations and implementation are not given here for the sake of brevity and can be found in (Chew & Liu 1996).

The governing equations of the acoustic medium inside and outside the artery are given as

$$\ddot{p} - \nabla^2 p = 0, \qquad\qquad\qquad \text{in } \Omega_f \qquad (2a)$$

$$p|_{t=0} = 0, \quad \dot{p}|_{t=0} = 0 \qquad\qquad \text{in } \Omega_f \qquad (2b)$$

$$\frac{\partial p}{\partial \mathbf{n}_f} = \rho_f \ddot{\mathbf{u}} \cdot \mathbf{n}_s, \qquad\qquad\qquad \text{on } \Gamma_{fs} \qquad (2c)$$

$$\frac{\partial p}{\partial \mathbf{n}_{rf}} = -\frac{\dot{p}}{c_f}, \qquad\qquad\qquad \text{on } \Psi_{RF} \qquad (2d)$$

where p is the fluid pressure, ρ_f is the density of the fluid surrounding the artery. Equation (2c) represents the boundary condition at the interface of the artery and the surrounding fluid and Eqn. (2d) describes the Sommerfeld radiation boundary condition on the truncated semi-infinite fluid medium. The variable Ω_f represents the fluid domain, Ψ_{RF} refers to the boundary where the radiation condition is applied, $\mathbf{n}_f$ is a unit vector normal to the fluid surface, and $\mathbf{n}_{rf}$ is the unit normal pointing outward of Ψ_{RF}. A schematic of the truncated artery and the surrounding fluid with the boundaries described in equations 1 and 2 is depicted in Fig. 1.
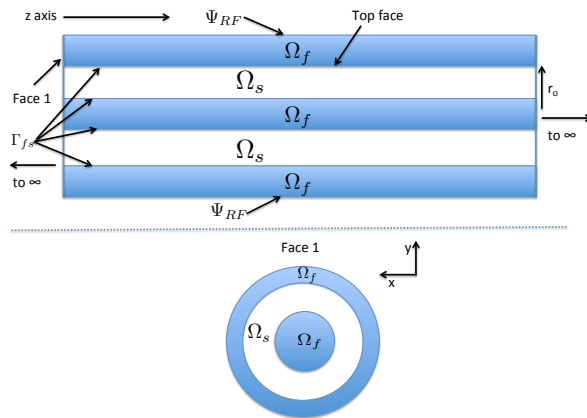
Figure 1. Figure describing the domains and boundaries for the artery problem. The blue region is the acoustic medium and the white region is the artery.

We used the Finite Element Method (FEM) to obtain approximate solutions to

the coupled boundary value problems described herein. Details of the FEM for ASI problems are omitted for brevity and can be found in (Everstine & Henderson 1990).

2.1.1. Group velocity We use group velocity measured along a path in the artery as the quantity of interest from which we identify geometric and material properties. This quantity of interest is commonly used in elasticity imaging due to its simplicity and ease of use (Bernal et al. 2011). In this section, we provide details for the calculation of group velocity from measured particle velocities along a path in an artery. Group velocity refers to the velocity with which a wave envelope propagates. In the current problem, we are interested in the group velocity of waves propagating on a path along the length of the artery. Traveling waves along such paths are easily measured with ultrasound transducers and hence are the focus of this work.

We will define a path along the length of the artery of as a set of coordinates given as (See Fig. 1)

$$\boldsymbol{T}(x, y, z) := \{r_o, 0, z\}, \tag{3}$$

where x, y are coordinates on the cross section of the artery and coordinate z is aligned along the length of the artery. r_o is the outer radius of the artery. We will next derive a approach to compute the group velocity along this path using the cross covariance of particle velocities.

Let $v_n(\boldsymbol{T}, t) := \dot{\mathbf{u}}(\boldsymbol{T}, t) \cdot \mathbf{n}_s$ be the normal particle velocity at time t and along path $\boldsymbol{T}$. The cross-correlation between two locations $\boldsymbol{T}_i := \{r_o, 0, z_i\}$ and $\boldsymbol{T}_j := \{r_o, 0, z_j\}$ for a given time difference τ is obtained as

$$C_{ij}(\tau) := \frac{\int_0^T [v_n(\boldsymbol{T}_i, t) - \hat{v}_n(\boldsymbol{T}_i)] \left[(v_n(\boldsymbol{T}_j, t + \tau) - \hat{v}_n(\boldsymbol{T}_j)) \right] dt}{K} \tag{4}$$

where T is the total time of wave propagation, K is a normalizing constant such that $C_{ii}(0) = 1$, and $\hat{v}_n(\boldsymbol{T}_i) := \int_0^T v_n(\boldsymbol{T}_i, t) dt / T$ is the mean velocity. The time delay t_{ij}^d is defined as the value of τ that maximizes the cross-correlation between positions $\boldsymbol{T}_i$ and $\boldsymbol{T}_j$ (Viola & Walker 2005), i.e.,

$$t_{ij}^d := \underset{\tau}{\operatorname{argmax}} \, C_{ij}(\tau). \tag{5}$$

The group velocity c_g is then found by solving the following least squares optimization problem.

$$c_g := \underset{v}{\operatorname{argmin}} \left\| v - \frac{\Delta z_{ij}}{t_{ij}^d} \right\|^2, \qquad \Delta z_{ij} := z_i - z_j \tag{6}$$

where $\| \cdot \|$ refers to the Euclidean norm.

2.1.2. Parameters of interest and sensitivity In this work, we assume arteries to be simple transversely isotropic cylindrical vessels. Hence, the main parameters of

interest consist, in general, of six independent material moduli, diameter, and thickness. The material parameters of interest are two Young's moduli; E_L, E_C; two Poisson ratios, ν_{LC}, ν_{RL}; and two shear moduli, G_{LC}, G_{RL}, where L, C and R represent longitudinal, circumferential, and radial directions, respectively. The geometry is described completely by its diameter (d) and thickness (h). Assuming incompressibility of the material, the Poisson ratios can be readily identified from the Young's moduli as (Bernal et al. 2011)

$$\nu_{LC} = \frac{1}{2} \tag{7}$$

$$\nu_{RL} = 1 - \frac{E_L}{2E_C} \tag{8}$$

Thus, we are left with a total of four (4) material parameters (i.e. E_L, E_C, G_{LC}, G_{RL}) plus the diameter and thickness to be identified.

We investigated the sensitivity of the group velocity to changes in the parameters of interest to determine the identifiability of the latter through an inverse problem approach. To this end, we carried out transient finite element simulations varying each parameter over a predetermined range, while fixing all others, and computed the group velocity. For the present case, E_C and E_L were sampled in the interval [50 kPa, 500 kPa], while G_{LC} and G_{RL} were sampled in the interval [20 kPa, 100 kPa]. The ranges were decided based on previously reported experimental results on artery moduli (Bernal et al. 2011). The diameter and thickness were varied within the ranges [2 mm, 9 mm] and [0.5 mm, 1mm], respectively.

Our sensitivity studies showed that group velocity was significantly sensitive to changes in the longitudinal modulus (E_L), thickness (h), and diameter (D). Although, we observed sensitivity of the group velocity to changes in circumferential modulus E_C, this sensitivity was less pronounced than that observed for the former three variables. On the other hand, group velocity was not sensitive to any significant extent to changes in the shear moduli G_{RL}, G_{LC}. Based on these observations, E_C, E_L, D and h were selected as the parameters of interest. Notice that since no sensitivity was observed to shear moduli, the group velocity is considered uninformative about these quantities and hence will be excluded from the inverse identification.

2.1.3. Model reduction In this section, we describe our approach for constructing surrogate models for arterial vessels immersed in a fluid. To this end, we employ sparse grid polynomial interpolation in order to construct maps that relate input parameters (e.g. geometric features and material parameters) to our main quantity of interest (i.e. group velocity).

We define a parameter vector $\boldsymbol{\xi} := \{E_L \ E_C \ h \ D\}^T$ for notational convenience. Let $v_n(\boldsymbol{T}, t, \boldsymbol{\xi})$ be the normal particle velocity along path $\boldsymbol{T}$ corresponding to a given set of parameters $\boldsymbol{\xi}$. We can represent the group velocity abstractly as

$$c_g(\boldsymbol{\xi}) = \mathcal{G}(v_n(\boldsymbol{T}, t, \boldsymbol{\xi})), \tag{9}$$

where $\mathcal{G}$ is a linear functional representing the operations described in Section 2.1.1.

Our main task herein is to devise a way to construct efficient and accurate approximations to $c_g(\boldsymbol{\xi})$. In this work, we will use polynomial interpolation to produce approximations $\hat{c}_g^h(\boldsymbol{\xi})$. A straightforward approach to this problem is to use tensor product representation of univariate polynomials along each parameter dimension. Using tensor products, Eqn. (9) is represented as

$$\hat{c}_g^h(\boldsymbol{\xi}) = \Phi_1(E_L) \otimes \Phi_2(E_C) \otimes \Phi_3(h) \otimes \Phi_4(D) \qquad (10)$$

where $\Phi_1(E_L)$, $\Phi_2(E_C)$, $\Phi_3(h)$ and $\Phi_4(D)$ are univariate polynomials. To create a polynomial interpolant using a conventional tensor product representation, the total number of points needed is $N_Q = \Pi_{i=1}^4 N_i$, where N_l is the number of points for a particular parameter. We can observe that the total number of points N_Q increases exponentially with the size of the parameter vector. This result is known as the curse of dimensionality as the computational cost of creating the polynomial interpolant also increases exponentially with the size of the parameter vector (Le Maître & Knio 2010).

To circumvent (at least in part) the curse of dimensionality, sparse tensorization is commonly used to create polynomial interpolants. Sparse interpolation grids use far fewer collocation points than those used by a conventional tensor product representation. In fact, sparse grids can reduce the number of collocation points needed for accurate interpolation by several orders of magnitude. This reduction in the number of interpolation or collocation points translates directly into computational savings as each point requires a finite element simulation.

A common approach to construct sparse interpolants is to use the Smolyak's interpolation algorithm (Smolyak 1963). The Smolyak's algorithm provides a methodology to create interpolation functions based on a coarse grid of points in a multidimensional space. The collection of this minimum number of points is called a sparse grid. For example a typical sparse grid in two dimensions is given in Fig. 2(a). Smolyak's algorithm interpolates using the sparse grid by extending univariate interpolation formulas to a multivariate case in a special way. For example, Fig. 2(b) shows interpolation of the function $\exp(-x^2 - y^2)$ using sparse grid and Smolyak's algorithm. Details of the Smolyak's algorithm have been omitted here for the sake of brevity and focus. The reader is referred to references (Le Maître & Knio 2010, Klimke 2006) for more information on general sparse grid interpolation.

We use the Smolyak's algorithm to create sparse grid interpolants of the group velocity with respect to the material moduli and geometric parameters. We describe this sparse interpolant (abstractly) as an operator $\mathcal{A} : \mathbb{R}^4 \mapsto \mathbb{R}$. That is, mathematically we define the group velocity as

$$\hat{c}_g^h := \mathcal{A}(\boldsymbol{\xi}), \qquad (11)$$

where $\hat{c}_g^h$ is the interpolated group velocity obtained via Smolyak's algorithm. Our goal is to use $\hat{c}_g^h$ in lieu of full finite element simulations in our inverse problem.

(a) Sparse grid points   (b) Sparse grid interpolation
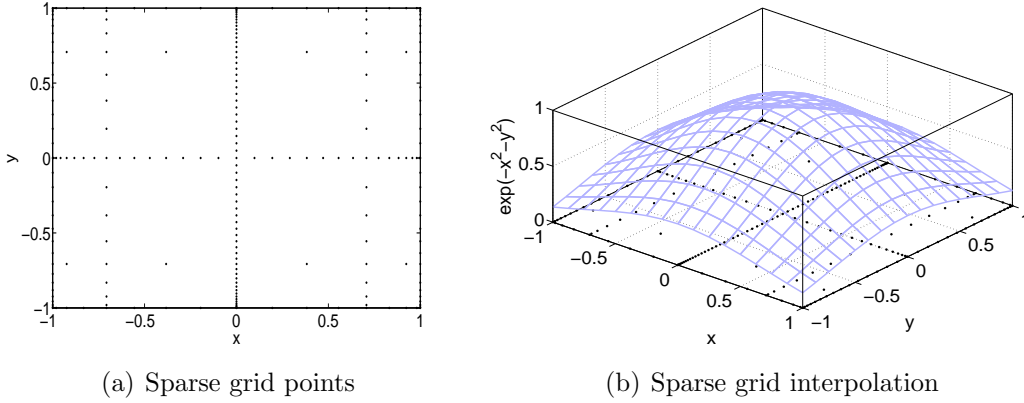
Figure 2. Figure showing (a) example of sparse grid points in two dimension and (b) interpolant created using the Smolyak's algorithm on the sparse grid in two dimensions for the example function $\exp(-x^2 - y^2)$,

An error estimate is used for assessing the accuracy of the interpolant. This error estimate is defined with respect to the level of interpolation, which in turn is a function of the number of points in the sparse grid (Chapter 3 in (Klimke 2006)). Let the interpolant created at $\boldsymbol{k}^{th}$ and $\boldsymbol{k}+\boldsymbol{1}^{th}$ levels of interpolation be given by $\hat{c}_g^{h,\boldsymbol{k}}$ and $\hat{c}_g^{h,\boldsymbol{k+1}}$, respectively. We determine a sufficiently accurate interpolant in $\hat{c}_g^{h,\boldsymbol{k}}$ if the following condition is met.

$$\|\hat{c}_g^{h,\boldsymbol{k+1}} - \hat{c}_g^{h,\boldsymbol{k}}\|_\infty < \epsilon, \tag{12}$$

where $\| \cdot \|_\infty$ refers to the maximum-norm. The parameter ϵ is a user-defined tolerance. It can be shown that as the level of interpolation increases, the error in interpolation decreases (Chapter 3 in (Klimke 2006)). However, the higher the level of interpolation the more collocation points are needed and, hence, the higher the computational cost of building the interpolant.

2.2. Algorithm for Creating the Surrogate Model

Now, we describe the algorithm for creating a surrogate model using sparse grid interpolation. First, we create a sparse grid where the axes are the components of the parameter vector $\boldsymbol{\xi^i}$, where $\boldsymbol{i}$ is the interpolation level. As mentioned before, the level of interpolation is directly related to number of points in the sparse grid. Let $\boldsymbol{\xi_k^i}$, $k = 1, \ldots, N_i$ represent the collocation points at level $\boldsymbol{i}$, where $N_{\boldsymbol{i}}$ is the total number of points. Each interpolation point, $\boldsymbol{\xi_k^i}$ on the sparse grid represents a four-dimensional vector of moduli and geometric features. Then, for each interpolation point, we perform a finite element simulation to obtain the particle velocity along path $\boldsymbol{T}$. The group velocity is then calculated for each interpolation point using Eqn. (9). The group velocity for the kth point at the $\boldsymbol{i}^{th}$ level is given by $c_{g,k}^{\boldsymbol{i}}$. Once the group velocity has been obtained for all interpolation points, we use Smolyak's algorithm to create an

interpolant of the group velocity. We terminate the surrogate creation when the error metric given in Eqn. (12) is met. The steps for the creation of a surrogate model are given in Algorithm 1.

Algorithm 1 Creation of the group velocity surrogate model.

Require: $\boldsymbol{\xi}_l, \boldsymbol{\xi}_u \in \mathbb{R}^4$ ▷ Upper and lower bounds.
Require: ϵ ▷ Error threshold.
 1: Set $E = \infty$ ▷ Initialize error metric.
 2: Set $\boldsymbol{i} = 1$ ▷ Initialize level.
 3: **while** $E > \epsilon$ **do**
 4:     Get points at $\boldsymbol{i}^{th}$ level, $\boldsymbol{\xi}_j^{\boldsymbol{i}} \in [\boldsymbol{\xi}_l, \boldsymbol{\xi}_u]$, $j = 1, \ldots, N_{\boldsymbol{i}}$
 5:     **for** $k = 1 \to N_{\boldsymbol{i}}$ **do**
 6:        $c_{g,k}^i = \mathcal{G}(v_n(\boldsymbol{T}, t, \boldsymbol{\xi}_k^{\boldsymbol{i}}))$ ▷ Group velocity calculation.
 7:     **end for**
 8:     $\hat{c}_g^{h,\boldsymbol{i}}(\boldsymbol{\xi}^{\boldsymbol{i}}) = \mathcal{A}(\boldsymbol{\xi}^{\boldsymbol{i}})$ ▷ Construct interpolant using Smolyak's algorithm.
 9:     **if** $\boldsymbol{i} > 1$ **then**
10:        Calculate $E = \|\hat{c}_g^{h,\boldsymbol{i}} - \hat{c}_g^{h,\boldsymbol{i}-1}\|_\infty$
11:     **end if**
12:     $\boldsymbol{i} = \boldsymbol{i} + 1$
13: **end while**

2.3. Inverse Problem Formulation

Let c_g^m denote the group velocity measured in an experiment. Then, the elastic moduli and geometry are reconstructed by solving

$$\hat{\boldsymbol{\xi}} = \underset{\boldsymbol{\xi} \in [\boldsymbol{\xi}_l, \boldsymbol{\xi}_u]}{\operatorname{argmin}} \|\hat{c}_g^h(\boldsymbol{\xi}) - c_g^m\|^2, \tag{13}$$

where $\boldsymbol{\xi}_l$ and $\boldsymbol{\xi}_u$ are the lower and upper bounds of $\boldsymbol{\xi}$, respectively, and $\hat{\boldsymbol{\xi}}$ is an optimal value of $\boldsymbol{\xi}$.

3. Numerical Results

In this section, we investigate the performance of the proposed sparse grid interpolation approach using numerical experiments with simulated data. To this end, we first constructed a 3D finite element model of an artery immersed in water. A Sommerfeld condition was used to model non-reflecting boundaries in both the artery and surrounding fluid. The density of both water and artery was taken as $1000 \, kg/m^3$. The artery was excited using a half sine pulse load with a duration of $406 \, \mu$s. Continuum 8-node hexahedral elements were used in all simulations and convergence studies were carried out to determine a suitable mesh for our computations. Transient analyses were carried out using 85 time steps of $40 \, \mu$s for a total time of 3.4 ms. All finite element simulations were performed using SIERRA/SDA from Sandia National Laboratories.

3.1. Construction of the surrogate model

A group velocity surrogate model was created using Algorithm 1. For this purpose, we used the `spinterp` toolbox in MATLAB® as described in (Klimke & Wohlmuth 2005). The circumferential (E_C) and longitudinal (E_L) moduli were sampled from the range $[60, 400]$ kPa, the thickness was sampled from the range $[0.3, 1]$ mm and the diameter from the range $[2, 7]$ mm. We used $\epsilon = 10^{-5}$ as the stopping interpolation error as per Algorithm 1. Using this error tolerance, the total number of interpolation points (i.e. finite element simulations) used to create the surrogate was 505.

To verify the accuracy of the surrogate model, we generated a test data set comprised of 25 random parameter vectors $\boldsymbol{\xi}$ sampled from the given moduli and geometry domains. For each parameter vector in the test set, we obtained a group velocity $\bar{c}_g$ from 3D FE simulations and the group velocity $\hat{c}_g^h$ from the surrogate model. We evaluated the error in the group velocity prediction as

$$e_{cg} = \frac{|\bar{c}_g - \hat{c}_g^h|}{\bar{c}_g} \times 100 \tag{14}$$

The average e_{cg} using the test data set was 8.47% and the maximum was 18.51%. It is important to keep in mind that this error does not translate into a commensurate error in the solution of the inverse problem (13) when a surrogate model is used. In fact, an effective surrogate model is one that preserves the topology of the objective function in the optimization problem such that the correct minimum is found despite the presence of errors in magnitude.

3.2. Inverse problem solution using simulated data

Simulated data was generated using the high fidelity 3D finite element model for different combinations of moduli and geometry as shown in Table 1. We first performed inversions for cases in which the data was not corrupted with noise, and then for cases in which Gaussian noise was added to the computed particle velocity before computing the group velocity. The corrupted data was generated as

$$\hat{v}_n(\boldsymbol{T}_i, t) = v_n(\boldsymbol{T}_i, t)(1 + \gamma \eta(\boldsymbol{T}_i, t)) \tag{15}$$

where $\hat{v}_n(\boldsymbol{T}_i, t)$ is the corrupted normal particle velocity, γ represents the noise level and $\eta(\boldsymbol{T}_i, t) \sim \mathcal{N}(0, 1)$ is a random variable drawn from a standard Normal distribution (independent for each time and position).

We solved the inverse problem in Eqn. (13) using the Optimization Toolbox in Matlab. Due to the computationally inexpensive nature of the surrogate model, we were able to use a global search algorithm (fminbnd in MATLAB). The results of the inversion without noise are reported in Table 1. It can be seen that the longitudinal modulus E_L, diameter D, and thickness h were identified with reasonable accuracy. However, the circumferential modulus E_C was not identified correctly. This latter

Table 1. Results of prediction of dimensions and moduli for numerical experiments.

	Parameters	Measured	Predicted	% error
	E_L (kPa)	100	90	10
	E_C (kPa)	120	70	41.2
Case 1	diameter (mm)	3.2	3.3	3.12
	thickness (mm)	0.40	0.48	20
	c_g (m/s)	5.79	5.75	0.69
	E_L (kPa)	100	93	7
	E_C (kPa)	120	67	44.2
Case 2	diameter (mm)	6.0	5.6	6.67
	thickness (mm)	0.70	0.74	5.17
	c_g (m/s)	6.10	5.90	3.27
	E_L (kPa)	100	89	11
	E_C (kPa)	120	65	45.8
Case 3	diameter (mm)	8.0	8.3	3.27
	thickness (mm)	0.90	0.86	4.44
	c_g (m/s)	5.72	5.81	1.58

Table 2. Results of prediction of dimensions and moduli for numerical experiments when noise was added to the group velocity data .

Noise level (p_c)	Parameters	Measured	Predicted	% error
	E_L (kPa)	100	112	12
	E_C (kPa)	120	64	46.67
1% noise	diameter (mm)	3.2	3.5	9.37
	thickness (mm)	0.40	0.50	25
	c_g (m/s) (with noise)	5.88	5.85	0.34
	E_L (kPa)	100	82	18
	E_C (kPa)	120	62	48.3
5% noise	diameter (mm)	3.2	3.9	21.87
	thickness (mm)	0.40	0.51	27.5
	c_g (m/s) (with noise)	5.90	5.88	0.33

result is in agreement with the fact that the group velocity displayed little sensitivity to E_C in our numerical studies. Table 1 also shows the group velocity predicted by the surrogate model at the identified parameters and the corresponding group velocity (actual) computed from 3D FE simulations. It can be seen that the group velocity values predicted by the surrogate are very close to those computed from the high fidelity simulations.

Table 2 shows the results of inversions performed on data polluted with Gaussian noise. It can be seen that as the noise level increases, the percentage error in prediction of the materials properties and dimension also increases, as expected. However, the

errors remain relatively low for all parameters, except for E_C as noticed previously.

4. Experimental Results

In this section, we study the performance of the proposed methodology using laboratory experiments. To this end, we conducted two separate experiments; one using a rubber tube and another using a porcine carotid artery immersed in saline solution subjected to different internal pressures. The proposed algorithm was used to reconstruct geometric and material properties from measured group velocity.

4.1. Description of the Experiments

A schematic of the experimental setup for the porcine carotid artery is shown in Fig. 3. The artery was immersed in a saline solution and its ends were fixed. A linear array transducer was used to apply an ultrasonic pulse excitation in the middle section of the artery and to measure the normal particle velocity along the top surface (see Fig. 1). The force duration was 406 μs. We report results for four different internal pressures: 20, 40, 60 and 80 mmHg.
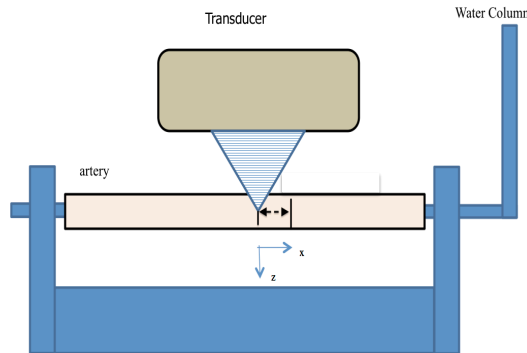
Figure 3. Experimental setup for the *in vitro* artery and rubber tube tests.

For the rubber tube experiment, we used the same setup as was used for the artery. The rubber tube was subjected to an internal pressure of 10 mmHg. At this pressure, the thickness of the tube was measured at 0.94 mm and the outer diameter was 6.5 mm. The data for the artery experiment was recorded with a sampling frequency of 7.5 kHz. The spatial sampling was performed with a spacing of 0.154 mm. For the rubber tubes, the sampling frequency was 5.68 kHz, and the spacing between two consecutive measurements was also 0.154 mm. The shear moduli of the rubber material in the tube was measured in a separate shear wave experiment and was estimated to be $G = 93$ kPa. Assuming incompressibility, the Young's modulus for the rubber tube was calculated as $E = 279$ kPa (i.e. $3 \times G$).

4.2. Inverse Identification Results

We processed all the experimental data using the same surrogate model and optimization procedure presented in Section 3. We first present the results obtained for the rubber tube. The value of group velocity obtained from the measured particle velocity was 6.98 m/s. Using our inverse problem framework, we estimated the geometric and material properties of the tube to be $E_L = 230 \ kPa$, $E_C = 90 \ kPa$, $D = 6.7$ mm, and $h = 0.96$ mm. Since the tube was isotropic, we expected that the values of E_C and E_L would be similar, which was not the case. This is a reflection of the lack of sensitivity of the group velocity with respect to E_C. Using the formula in Eqn. (14), we estimated the respective errors to be 17%, 67%, 3% and 2%. Furthermore, we performed a 3D FE simulation (with the estimated parameters) and determined the group velocity to be 6.54 m/s, which corresponds to a relative error of 6.3% with respect to the experimentally measured value. We can see that, with the exception of E_C, all parameters were estimated with good accuracy.

We also compared dispersion curves obtained from the 3D FE simulations corresponding to the identified parameters with the dispersion curves obtained from the experimental data. To get the dispersion curves, we performed a two-dimensional (2D) fast Fourier transform (FFT) of the normal particle velocity along the measurement path on the artery (see Section 2.1.1). We used the procedure described in (Bernal et al. 2011) to obtain the dispersion curves from the 2D FFT. Figure 4.2 shows a comparison of the experimental and simulation dispersion curves for the rubber tube. We can observe that the dominant modes obtained from the experimental data and optimized material properties are close to each other over a wide frequency range.
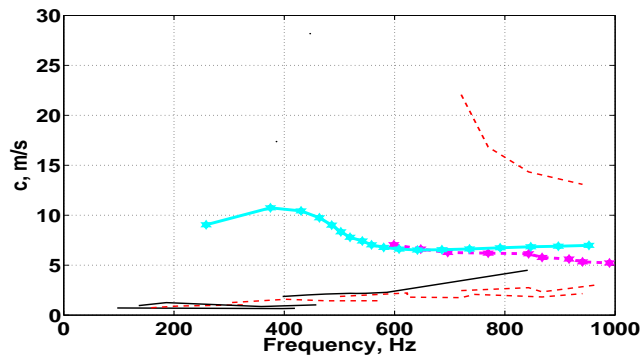
Figure 4. Comparison of dispersion diagrams obtained from the data and from post processing optimized material properties and geometry for the rubber tube. The solid lines represent dispersion curves obtained from the experiment and the dashed lines represent dispersion curves obtained from a 3D FE simulation using the optimized material properties and dimensions. The cyan line is the dominant dispersion mode obtained from the experimental data and the magenta line is the dominant mode obtained from the FE simulation.

Next we consider the inverse identification of material properties and dimensions for the excised artery. The results are summarized in Table 3, which shows that the recovered diameter and thickness closely approximate the measured values. We can observe from this table that the maximum relative error was 11.59% and occurred for the diameter estimate in the 80 mmHg case.

Table 3. Results for inverse identification of artery geometry at different hydrostatic pressures. D and h refer to diameter and thickness respectively.

Pressure	Measured D (mm)	Predicted D (mm)	% error	Measured h (mm)	Predicted h (mm)	% error
20 mmHg	3.0	3.2	6.67	0.70	0.75	7.14
40 mmHg	3.1	3.5	12.9	0.64	0.70	9.37
60 mmHg	3.3	3.4	3.38	0.59	0.63	5.72
80 mmHg	3.6	3.6	0.73	0.51	0.57	11.59

The recovered material properties and group velocities are presented in Table 4. The predicted or identified group velocities ($\hat{c}_g$) were obtained from 3D FE simulations using the identified material and geometric properties. Table 4 shows that the predicted group velocities are very close to the group velocities ($\bar{c}_g$) obtained from the experimental data. As for the prediction of material properties, the values obtained for E_L were consistent with those reported in (Bernal et al. 2011). However, the E_C values obtained seem to be inaccurate, which is consistent with the findings reported for the rubber tube and the numerical experiments presented in Section 3.2.

Table 4. Results for inverse identification of artery moduli and group velocity values.

Pressure	Measured $\bar{c}_g$	Predicted $\hat{c}_g$	% error	Predicted E_C (kPa)	Predicted E_L (kPa)
20 mmHg	5.46	5.60	2.6	102	230
40 mmHg	5.77	6.02	4.3	95	240
60 mmHg	6.03	6.15	2.0	90	256
80 mmHg	6.29	6.35	0.95	88	270

Figure 5 compares the dispersion curves obtained from the experimental data and those obtained from 3D FE simulations using the recovered moduli and geometry. A close agreement is observed in the dominant modes of the data and optimized material properties, for arteries at 20, 40 and 60 mmHg hydrostatic pressures. Also, for lower frequencies and low phase velocity, the non-dominant dispersion curves are in close agreement. The discrepancy in the phase velocity curves for the 80 mmHg case was larger than for the other cases. However, the identified diameter and thickness were accurately estimated and the longitudinal modulus fell the expected trend (i.e. value increased with pressure).
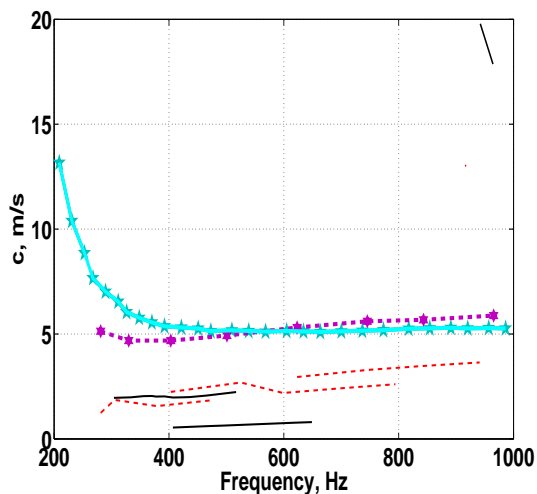
(a) Artery at pressure 20 mmHg
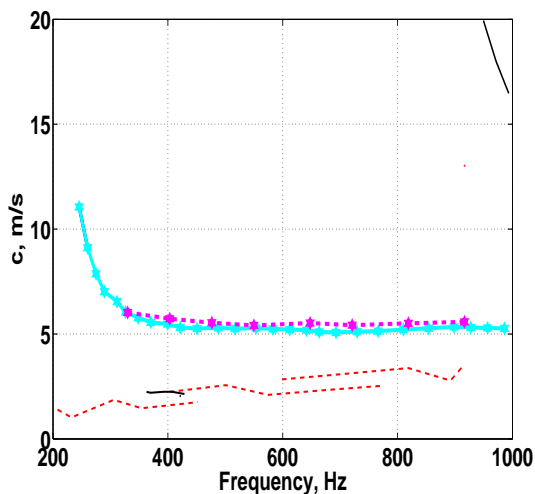
(b) Artery at pressure 40 mmHg
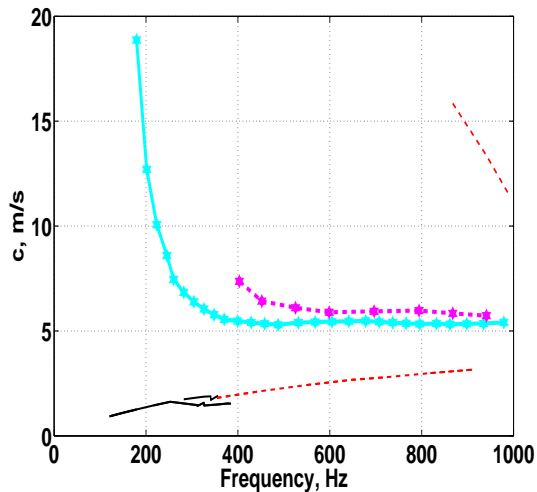
(c) Artery at pressure 60 mmHg
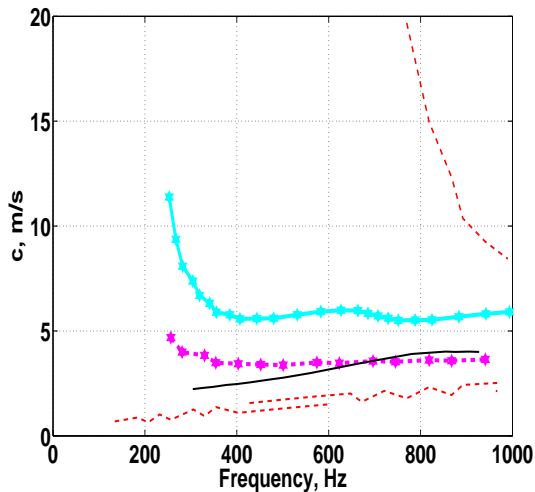
(d) Artery at pressure 80 mmHg

Figure 5. Comparison of dispersion diagrams obtained from the experimental data and 3D FE simulations using the recovered material properties and geometry. The solid lines represent dispersion curves obtained from the experimental data and the dashed lines represent dispersion curves obtained from FE simulations. The cyan line is the dominant mode obtained from the experimental data and the magenta line is the dominant mode obtained from the FE simulations.

5. Concluding Remarks and Future Work

The prediction of thickness, diameter, and material properties are of paramount importance in the characterization of cardiovascular diseases. In this work, we presented a novel approach for the fast and noninvasive identification of material properties and geometry of arteries excited by an ultrasonic pulse. The main algorithm used a Smolyak's sparse grid collocation technique to create a surrogate model mapping the moduli and dimensions to the group velocity. Once a surrogate model is created, the identification process can be carried out in near real time across different specimens and internal pressures. The main advantage of the proposed approach is that the surrogate model combines computational speed with knowledge of the fundamental physics of the underlying wave propagation problem.

We applied the proposed inversion methodology to obtain longitudinal and circumferential moduli as well as thickness and diameter in an excised artery subjected to different internal pressures and a silicon tube. It was found that the proposed method could effectively identify the longitudinal modulus, diameter and thickness. However, the circumferential modulus could not be identified. The inaccuracy in the identification of E_C can be attributed to the fact that the group velocity measured along a longitudinal path seems to be relatively insensitive to changes in this parameter. It seems plausible that devising experiments that capture wave motion in the circumferential direction would yield more accurate reconstructions of E_C; a direction that would be pursued in the near future.

To apply the current methodology *in vivo*, the high fidelity and surrogate models have to incorporate surrounding tissue and viscoelastic effects (both in the artery and the surrounding tissue). These features can be naturally incorporated in the proposed sparse grid collocation framework. However, these model extensions are expected to increase the dimensionality of the problem, and hence the computational cost of constructing the surrogate model. Yet, this increase in computational cost can be mitigated by the used of sparse grids. Furthermore, due to their uncoupled nature in collocation approaches, high-fidelity simulations can be carried out straightforwardly in parallel. Moreover, surrogate models are built offline and can be used across many different inversion cases in near real-time, compensating for the initial high-computational cost.

Finally, another direction that will be pursued in future research is the development of adaptive strategies for constructing the surrogate model. The basic premise would be to start with a coarse grid of parameters (e.g. geometry and material) and choose collocation points according to the sensitivity of a quantity of interest along different coordinates (i.e. parameters). Similar approaches have been successfully used for uncertainty quantification (Ganapathysubramanian & Zabaras 2007).

6. Acknowledgments

References

Aguilo M A, Aquino W, Brigham J C & Fatemi M 2010 *Medical Imaging, IEEE Transactions on* **29**(4), 1012–1021.

Arridge S R & Hebden J C 1997 *Physics in Medicine and Biology* **42**(5), 841.

Bernal M, Nenadic I, Urban M W & Greenleaf J F 2011 *The Journal of the Acoustical Society of America* **129**(3), 1344–1354.

Bishop C M 2006 *Pattern recognition and machine learning* Vol. 1 springer New York.

Blacher J, Pannier B, Guerin A P, Marchais S J, Safar M E & London G M 1998 *Hypertension* **32**(3), 570–574.

Brigham J, Aquino W, Mitri F, Greenleaf J & Fatemi M 2007 *Journal of Applied Physics* **101**(2), 023509.

Brigham J C & Aquino W 2007 *Computer Methods in Applied Mechanics and Engineering* **196**(45), 4561–4576.

Chew W & Liu Q 1996 *Journal of Computational Acoustics* **4**(04), 341–359.

Cockcroft J R, Wilkinson I B, Evans M, McEwan P, Peters J R, Davies S, Scanlon M F & Currie C J 2005 *American journal of hypertension* **18**(11), 1463–1467.

Couade M, Pernot M, Prada C, Messas E, Emmerich J, Bruneval P, Criton A, Fink M & Tanter M 2010 *Ultrasound in medicine & biology* **36**(10), 1662–1676.

Davis P H, Dawson J D, Mahoney L T & Lauer R M 1999 *Circulation* **100**(8), 838–842.

Deng Y M & Edwards K 2007 *Materials & design* **28**(1), 131–139.

Everstine G C & Henderson F M 1990 *The Journal of the Acoustical Society of America* **87**(5), 1938–1947.

Ganapathysubramanian B & Zabaras N 2007 *Journal of Computational Physics* **225**(1), 652–685.

Klimke A W 2006 Uncertainty modeling using fuzzy arithmetic and sparse grids PhD thesis Universität Stuttgart.

Klimke A, Willner K & Wohlmuth B 2004 *International Journal of Uncertainty, Fuzziness and Knowledge-Based Systems* **12**(06), 745–759.

Klimke A & Wohlmuth B 2005 *ACM Transactions on Mathematical Software (TOMS)* **31**(4), 561–579.

Konofagou E, Lee W N, Luo J, Provost J & Vappou J 2011 *Annual Review of Biomedical Engineering* **13**(1), 477–505.

Le Maître O P & Knio O M 2010 *Spectral methods for uncertainty quantification: with applications to computational fluid dynamics* Springer.

Luo J, Fujikura K, Tyrie L S, Tilson III M D & Konofagou E E 2009 *IEEE Transactions on Medical Imaging* **28**(4), 477–486.

Luo J, Li R & Konofagou E 2012 *Ultrasonics, Ferroelectrics, and Frequency Control, IEEE Transactions on* **59**(1), 174–181.

Nobile F, Tempone R & Webster C G 2008 *SIAM Journal on Numerical Analysis* **46**(5), 2309–2345.

Oberai A A, Gokhale N H & Feijoo G R 2003 *Inverse Problems* **19**(2), 297.

Polak J F, Pencina M J, Pencina K M, O'Donnell C J, Wolf P A & D'Agostino Sr R B 2011 *New England Journal of Medicine* **365**(3), 213–221.

Rosario D E, Brigham J C & Aquino W 2008 *Ultrasonics* **48**(6), 547–552.

Smolyak S A 1963 *Dokl. Akad. Nauk SSSR* **4**(123), 240–243.

Viola F & Walker W F 2005 *Ultrasonics, Ferroelectrics and Frequency Control, IEEE Transactions on* **52**(1), 80–93.

Xiu D & Hesthaven J S 2005 *SIAM Journal on Scientific Computing* **27**(3), 1118–1139.

Zhang X, Kinnick R R, Fatemi M & Greenleaf J F 2005 *Ultrasonics, Ferroelectrics and Frequency Control, IEEE Transactions on* **52**(4), 642–652.